This is a preprint, the final version is subject to change, of the American Mineralogist (MSA)
Cite as Authors (Year) Title. American Mineralogist, in press.
(DOI will not work until issue is live.) DOI: http://dx.doi.org/10.2138/am.2013.4145

Revision 3

Acoustic velocity measurements for stishovite across the post-stishovite phase transition under deviatoric stress: Implications for the seismic features of subducting slabs in the mid-mantle

Yuki ASAHARA[*,1,#], Kei HIROSE[2, 3], Yasuo OHISHI[4], Naohisa HIRAO[4], Haruka OZAWA[3], Motohiko MURAKAMI[5]

[1]Osaka University, Toyonaka 560-0043, Japan (*correspondence: asahara.y@m.tohoku.ac.jp)

[2]Tokyo Institute of Technology, Meguro, Tokyo 152-8551, Japan

[3] IFREE/JAMSTEC, Yokosuka, Kanagawa 237-0061, Japan

[4]JASRI/SPring-8, Sayo, Hyogo 679-5198, Japan

[5]Tohoku University, Sendai 980-8578, Japan

[#]Present address; Tohoku University, Sendai 980-8578, Japan

ABSTRACT

The acoustic velocity in polycrystalline stishovite across the post-stishovite phase transition was measured by Brillouin scattering in the pure SiO_2 system at room temperature under deviatoric stress. High-pressure synchrotron X-ray diffraction data were also collected at SPring-8. A linear fit to the symmetry-breaking strain values and the pressure of the transverse velocity minimum indicate a transition pressure between 25 and 35 GPa, which is about 20 GPa lower than that under hydrostatic conditions. The transverse velocity dropped by about 3% at around 25 GPa in this study. This is much smaller than the prediction from ab initio calculations that a transverse velocity reduces by approximately 60% at around 50 GPa under hydrostatic conditions. The results of the present study indicate that the deviatoric stress lowers transition pressure and reduces acoustic velocity change associated with the post stishovite phase transition. Sedimentary and mid ocean ridge basalt (MORB) layers in a subducting slab are likely sites for finding stishovite and its high-pressure polymorphs in the deep earth. Seismic observations of deep earthquakes occurring in subducting slabs indicate the existence of considerable stress in downgoing slabs. This study suggests that nonhydrostatic deviatoric stress is one of the possible reasons for the absence of general seismic features in subducting slabs corresponding to

1500 km depth that can be directly related to the post-stishovite phase transition. The phase transition of stishovite under deviatoric stress, which occurs at shallower depths, can affect the local seismic scattering structures and the rheological behavior of a subducting slab in the mid-lower mantle region.

Keywords: HIGH PRESSURE STUDIES: stishovite, acoustic velocity, post-stishovite transition, deviatoric stress, subducting slab

INTRODUCTION

Silica (SiO_2) is one of the major constituents of the earth's crust, and significant amounts of silica and silicates are transported to the deep earth by subducting slabs. Stishovite, a six-coordinated high-pressure polymorph of silica, is considered to be an important constituent of subducted oceanic basalts and sediments in the earth's deep interior. Stishovite exhibits the tetragonal rutile structure and transforms to the orthorhombic $CaCl_2$ structure above 50 GPa in the pure SiO_2 system (e.g., Tsuchida and Yagi 1989; Kingma et al. 1995; Andrault et al. 1998; Hemley et al. 2000; Andrault et al. 2003). This has been thought to be a classic displacive transition. According to theoretical models, the phase transition is triggered by the lattice instability of the soft transverse acoustic mode associated with the shear elastic constant; $(c_{11}-c_{12})/2$. A strong change in elastic properties is expected across the transition (e.g., Cohen 1992). Karki et al. (1997) reported that the shear wave velocity (V_S) decreases by 60% and the anisotropy increases by a factor of five prior to the transition from the tetragonal rutile structure to the orthorhombic $CaCl_2$ structure based on athermal first-principle calculations. They reported that the post-stishovite phase transition may cause discontinuous change in the shear wave velocity. Conversely, using a

Landau free energy expansion, Carpenter et al. (2000) suggested that the variation in the transverse and longitudinal velocities might exhibit a dip instead of a discontinuity in the vicinity of the transitional pressure. For this considerable expected character, the nature of the post-stishovite phase transition has been the focus of much research in condensed-matter physics and earth science.

The reported values for the transition pressure widely ranges from 40 to 90 GPa. Such scattering possibly resulted from the difficulty in phase identification and the choice of pressure scales, and the effect of deviatoric stress. It is known that the deviatoric stress affects the phase transformation pressures of crystals (e.g., Akaogi and Akimoto 1977); in particular, the effect of deviatoric stress is considered to be strong for the post-stishovite phase transition. Dubrovinsky and Belonoshiko (1996), using molecular and lattice dynamics, suggested that deviatoric stress of about 1.5–2.5 GPa is sufficient to trigger structural transformation occurred at much lower pressures than that under hydrostatic conditions. Hemley et al. (2000) conducted high-pressure experiments using single-crystal stishovite in a hydrogen pressure medium and observed hysteresis of transition; the transition between stishovite and the $CaCl_2$-structured phase occurred at 58 GPa along the compression path and at 40 GPa along the decompression path. The hysteresis of transition

77 indicates weak first-order character, and it may indicate a finite value of C_{11}-C_{12} at
78 transition pressure. It is also possible that the hysteresis was a result of small deviatoric
79 stress remained in the sample. Andrault et al. (2003) conducted powder X-ray diffraction
80 experiments for SiO_2 up to 130 GPa using the laser annealing technique and a NaCl
81 pressure medium. They synthesized stishovite at around 12 GPa in the diamond anvil cell
82 and annealed the sample before conducting all measurements at 2300 K, and checked the
83 full width at half maximum (FWHM) of the X-ray diffraction lines to confirm whether the
84 stress was relaxed. They observed the transition pressure around 60 GPa. They also
85 suggested that the post stishovite transition is essentially second order from strain and
86 thermal energy analysis. Radial X-ray diffraction experiments and stress analyses across the
87 post-stishovite phase transition under nonhydrostatic compression were conducted by Shieh
88 et al. (2002). They used synthesized stishovite powder as a starting material and no pressure
89 medium. The differential stress of stishovite was observed to be 4.5 GPa below 40 GPa,
90 and was found to decrease in a pressure range of 40–50 GPa. They also observed that the
91 difference between the volumes obtained across the maximum and minimum strain axes
92 increased above 20 GPa. It indicates that lattice deformation of stishovite started around 20
93 GPa, although the differential stress in the sample reached a minimum around 50 GPa.

From inversion of measured lattice strains, they suggested that elastic instability occurs in stishovite near 50 GPa.

The elastic constants of stishovite were measured at ambient conditions (Weidner et al. 1982; Brazhkin et al. 2005), and up to 12 GPa (Jiang et al. 2009) by Brillouin spectroscopy. However, there are no experimental acoustic velocity data for pure stishovite across the transition. Lakshtanov et al. (2007) conducted simultaneous Brillouin scattering and synchrotron X-ray diffraction measurements for hydrous alumina-bearing stishovite across the post-stishovite transition. The transition pressure for stishovite with impurities of 6 wt% Al_2O_3 and 0.24 wt% H_2O dropped to approximately 25 GPa. The acoustic shear velocity near the [110] phonon direction decreased by approximately 11%. In this phonon direction, the elastic shear modulus should vanish approaching the transition pressure, i.e., V_S becomes zero. The deviation from the [110] direction and the presence of impurities may be the reasons for the shear velocity not completely reaching zero at the transition pressure.

In this study, we measured acoustic velocities in pure, polycrystalline stishovite samples under nonhydrostatic conditions. In principle, acoustic velocity measurements under hydrostatic conditions should be performed to clarify the nature of the post-stishovite transition in the pure SiO_2 system. However, this is technically challenging and the

111 experimental pressure has been limited to 12 GPa (Jiang et al. 2009). A method of
112 measuring the acoustic velocities of stishovite and other lower-mantle phases under
113 quasi-hydrostatic conditions at high temperatures and high pressures is required. With this
114 in mind, we conducted acoustic velocity measurements of stishovite under nonhydrostatic
115 conditions in process of developing method. Sedimentary and MORB layers in the
116 subducting slab are plausible sites for high-pressure silica polymorphs to exist in the deep
117 earth. Deep earthquakes reveal that subducting slabs are under considerable stress in the
118 mantle. The present study may give insight on the seismic features and physical properties
119 of subducting slabs.
120
121
122 **EXPERIMENTAL PROCEDURE**
123 We synthesized a polycrystalline stishovite sample for Brillouin acoustic velocity and
124 X-ray diffraction measurements by sintering SiO_2 reagent powder at 20 GPa and 1500 K
125 using a Kawai-type multi-anvil apparatus. The sample was sufficiently transparent for
126 Brillouin scattering. The synthesized pellet was analyzed using a scanning electron
127 microprobe equipped with an electron dispersive spectrometer, and with an infrared

spectrometer. The pellet consists of pure SiO_2 and has an OH concentration of approximately 20 ppm. X-ray diffraction was measured with a microfocused X-ray diffractmeter (Rigaku) with an anticathode of Cu; a wavelength of 1.5418 Å. The average grain size of the sintered pellet is about 1 μm. The pellet was double-side polished to a final thickness of about 40 μm, and cut with a diamond saw to about 80 μm square. The polycrystalline chip was loaded between thin NaCl pellets in a hole in a pre-indented rhenium gasket and confined in a symmetric diamond anvil cell with a 60° angular aperture. Two beveled diamonds with 200 μm culets were used as anvils. A photograph of the sample is shown in Figure 1. The diameter of the sample chamber was about 100 μm. NaCl was used as the pressure medium and as a pressure gauge. The sample was compressed at 2–3 GPa intervals and was heated at 423 K in a vacuum oven to reduce the deviatoric stress in the sample chamber to below 10 GPa. Above 10 GPa, the compressed sample was heated using a CO_2 laser with an injected power of 20–30 W for about 60 s to reduce the deviatoric stress. We heated the sample to temperatures well below the condition at which irradiation started to prevent grain growth because the Brillouin signal is sensitive to crystallographic orientation (e.g., Shimizu et al. 1995; Baer et al. 1998). After heating, the pressure was measured using the Raman peak shift of diamond (Akahama and Kawamura 2006), and

145 then the Brillouin scattering data were collected.

146 Brillouin scattering was performed with the system installed at SPring-8/ BL10XU
147 (Ohishi et al. 2008). A six-path tandem Fabry-Perot interferometer was used to collect the
148 Brillouin spectra. A diode-pumped laser with a wavelength of 532 nm was used as the
149 incident probe beam, and was focused on the sample to a spot size of approximately 20 μm
150 in diameter. All measurements were performed in a symmetric scattering geometry with an
151 external scattering angle (θ) of 49.0–50.7°, which was calibrated with a borosilicate crown
152 optical glass (BK7; Yoneda and Song 2005) before measurements. Three separate series of
153 experiments were conducted for the Brillouin scattering and X-ray diffraction
154 measurements. The first series were performed along the compression path, and the second
155 along both the compression and decompression paths. Two chips of polycrystalline
156 stishovite were used for the first and second series respectively. These were cut from the
157 same sintered pellet. NaCl was used as a pressure medium. The collection of Brillouin
158 scattering spectra was conducted at 1–65 GPa in the first and second series of experiments.
159 The X-ray diffraction measurements were conducted at pressures of 1, 40, and
160 approximately 60 GPa after the Brillouin scattering measurements on the same loading
161 conditions respectively. The chip recovered from the second set of experiments was loaded

with a small ruby sphere and a mixture of methanol–ethanol–water (in proportions of 16:3:1 by volume) for the third set of experiments to examine the effect of deviatoric stress on the sample during the high-pressure experiment. X-ray diffraction measurements were performed at pressure ranged 4.7–15.6 GPa along the compression path in the third series of experiments. We conducted Brillouin scattering measurements on the recovered sample only at 4.7 GPa. The recovered sample was partly deteriorated by the green laser injection, therefore, we didn't measure Brillouin scattering of the sample at higher pressures.

We collected Brillouin spectra from three or four different positions and χ angles (χ angle: the angle rotated around the compression axis of the diamond anvil cell) at fixed pressure conditions. The number of grains probed at a given pressure is roughly estimated about 1800–3200 from diameter of incident laser (20 μm) and sample thickness (30-40μm) under pressure, and number of measurements. We averaged the data at the same pressure conditions from the first and second series of experiments to ensure a representative average of acoustic velocity in the polycrystalline sample. The uncertainties of the individual velocity data were ±120 m/s (less than 1%) for V_p and ±80 m/s for V_s (less than 1.2%).

The X-ray diffraction measurements were conducted in four different experimental

179 periods, and the experimental conditions and results are summarized in Table 1. The
180 angle-dispersive X-ray diffraction spectra were collected using a CCD camera or an
181 imaging plate. The incident X-ray beams were monochromized to wavelengths of 0.4130,
182 0.4135, 0.4136, and 0.4157 Å respectively for each experimental period. The X-ray beam
183 was collimated to 15 or 30 μm in diameter. The collection time for each X-ray diffraction
184 measurement was about 120–240 s.

185 The pressure deviations of the different pressure scales, i.e., Raman frequency shift of
186 the diamond and NaCl volume (Brown 1999, for B1 structure; Sakai et al. 2011, for B2
187 structure) and ruby fluorescence (Mao et al. 1978), were within ±3 GPa above the pressure
188 of 15 GPa. This includes the uncertainty of the pressure determination and the pressure
189 gradient in the sample chamber. The relationship between the pressures obtained with the
190 diamond Raman scale and those obtained using the other scales are shown in Figure 2.
191 Only the (110) diffraction from the B2-structured NaCl was observed. Therefore, we did
192 not use B2-structured NaCl as a pressure scale but used as a pressure gauge showing the
193 pressure gradient within the sample chamber. We used the B1-NaCl and the ruby scale
194 below 20 GPa, and the diamond Raman scale above 20 GPa to determine the experimental
195 pressure.

196

197

198 **RESULTS**

199 The fine circular two-dimensional X-ray diffraction image obtained in this study
200 indicates that the sample was initially an isotropic aggregate with no preferred orientation
201 (see supplementary figure). The variations in measured acoustic velocity along χ angles
202 were about 5.2 % for longitudinal velocity (V_P) and 3.8% for transverse velocity (V_S) at 1
203 GPa (NaCl-B1 pressure gauge). These variations were less than 1.4 % for V_p and less than
204 1.1 % for V_S at higher pressures. There was no clear correlation between velocity variation
205 and χ angle. Relatively large variations in velocity at 1 GPa might indicate that the sample
206 was not compacted well yet at that pressure. A representative Brillouin spectrum is shown
207 in Figure 3. The longitudinal acoustic velocities and transverse acoustic velocities obtained
208 as a function of pressure are shown in Figure 4. It is observed that the transverse velocity
209 reaches a minimum between 20 GPa and 30 GPa, whereas this is not observed for
210 longitudinal velocity. The V_p signal of stishovite always overlapped the V_s signal of
211 single-crystal diamond, and therefore, the peak fitting has rather large uncertainties (less
212 than 1%). The standard deviation of an average of measured velocities obtained from

different series of experiments with NaCl pressure medium was less than 2% except for the value obtained at 20 GPa along compression paths (2.7% for V_S). Measured velocities obtained during compression and decompression were comparable. It indicates that grain size reduction under pressure did not occur to a level that causes velocity reduction (Marquardt et al. 2011) in the present experiments. When a mixture of methanol–ethanol–water was used as a pressure medium, the measured velocity for the recovered sample was comparable with those obtained at first and second series of experiments. The sample was deteriorated by the green laser at the first Brillouin scattering measurement, and therefore the Brillouin spectrum was collected only at 4.7 GPa for the third series of experiment.

The representative integrated X-ray diffraction profiles collected at the pressures of 1, 16, 39, and 60 GPa are shown in Figure 5. The (211) of stishovite splits into two peaks above 30 GPa (i.e., (121) and (211) of the $CaCl_2$-structured phase), which indicates that the rutile-type structure is distorted to the $CaCl_2$-type structure (e.g., Andrault et al. 1998). A NaCl-B2 pressure gauge indicated that the pressure difference between the center and the edge of the stishovite pellet was about 2 GPa at 39 GPa. The broad FWHM in the X-ray diffraction profiles (Fig. 5) also indicate that a certain amount of stress remained after

annealing.

It is known that the identification of the rutile-type structured phase and the $CaCl_2$-type structured phase is difficult from an X-ray diffraction profile due to the similarity and small splitting. Therefore, we calculated the symmetry-breaking strain (Carpenter et al. 2000) to determine the transition pressure. The spontaneous strains e_1–e_3 for the tetragonal → orthorhombic transition are defined as $e_1 = (a - a_0)/a_0$, $e_2 = (b - a_0)/a_0$, and $e_3 = (c - c_0)/c_0$, where a, b, and c are the lattice parameters of the orthorhombic phase, and a_0 and c_0 are the lattice parameters of the tetragonal phase, extrapolated into the stability field of the orthorhombic phase [$a_0 = (a \times b)^{0.5}$]. The symmetry-breaking strain is $(e_1 - e_2) = (a - b)/a_0$. The square of the measured symmetry-breaking strain is shown as a function of pressure in Figure 6 along with previous results (Andrault et al. 2003). The linear fit to the data, $(e_1 - e_2)^2$ are greater than zero, gives a transition pressure of 35 GPa. This transition pressure is considerably lower than the values which reported in previous X-ray diffraction studies for single crystal SiO_2 (stishovite) under quasi-hydrostatic conditions (Hemley et al. 2000); about 50 GPa, and for polycrystalline SiO_2 (stishovite) using the laser annealing method (Andrault et al. 2003); about 60 GPa. The unit cell volume and lattice parameters as a function of pressure determined in this study as well as in previous studies are shown in

Figure 7. The unit cell volume measured in this study deviated by approximately 3.2% over 30 GPa from the compression curve of stishovite, which was previously reported under hydrostatic conditions. This indicates that the nonhydrostatic effect became severer over 30 GPa. The compressibility of the c-axis measured in this study is almost comparable (within 0.3%) to that under hydrostatic conditions, whereas the a-axis is less compressible than that under hydrostatic conditions. The linear fit to the symmetry-breaking strain and the transverse velocity minimum indicate that the transition pressure is in the range of 25–35 GPa in the present study.

We conducted the line breadths analyses to get information about microstress with following procedure. Similar analyses have been conducted on energy dispersion X-ray profiles (e.g., Gerward et al. 1976; Weidner et al. 1998). The line breadths due to particle size, β_S, and distortions, β_D, in angle-dispersive diffraction are expressed with following equations (Klug and Alexander 1974);

$$\beta_S(2\theta) = \frac{K\lambda}{L\cos\theta} \quad (1)$$

$$\beta_D(2\theta) = 4e\tan\theta \quad (2)$$

, where K is the Sherrer constant, λ is the X-ray wavelength, θ is the scattering angle, L is the average crystalline size, and e is the approximate upper limit of strain.

With the assumptions as to the shape of the broadening profile due to crystalline size and strain, the observed breadths, B, in the case of Lorentzian (Cauchy type) profiles is given by

$$B(2\theta) = \beta_S(2\theta) + \beta_D(2\theta) \quad (3)$$

The effect of grain size of 1 μm, which obtained by SEM analyses in present study, is small and it is easily hidden in the effect of instrumental contribution. If we apply equation 1 (Sherrer equation) to estimate grain size of around 1 μm, we need a careful evaluation of instrumental broadening. Brillouin scattering result suggests that apparent grain size reduction didn't occur in present experiment. Therefore, we use this equation for the evaluation of instrumental contribution in present study. We assume instrumental broadening can be included in the term of β_S as a constant, and crystalline size L is a constant in present study, then equation 3 can be written

$$B(2\theta) = \frac{a\lambda}{\cos\theta} + 4e\tan\theta \quad (4)$$

, where a is a constant including the effects of instrumental reflection and crystalline size.

Figure 8 shows the observed breadths of stishovite plotted against 2 theta at 1.1 GPa obtained in this study. We used a FWHM as for a peak breadth in present study. We

obtained $a = 9.8 \times 10^6 \pm 0.8 \times 10^6$ m^{-1}, and average upper limit of strain $e = 9.0 \times 10^{-4} \pm 0.7 \times 10^{-4}$ by fitting the FWHM data with equation 4. We can obtain upper limits of strain from independent peaks with the obtained value of a and equation 4. Figure 9a and 9b show upper limits of strain from independent diffraction peaks plotted against d value and pressure respectively. Uncertainty of the values is approximately 9%. Large deviation of the strain values from hkl = (101) compared to those from the other directions are the result of contamination of hkl = (011) above 30 GPa. Except for the contaminated hkl = (101), the deviation between the strain values of hkl = (110) and (111) increases with increasing pressure above 30 GPa. The deviation may indicate that the deviatoric stress in the polycrystalline stishovite increases severely with increasing pressure above 30 GPa. To be exact, we need strain data and elastic constants for all independent orientation to obtain deviatoric stress. We note the values of the average upper limit of strain multiplied bulk modulus because the value may indicate deviatoric stress range on the sample: The values are 2.3 GPa, 4.4 GPa, and 7.0 GPa at the experimental pressures of 16 GPa, 39 GPa, and 64 GPa, respectively. The bulk modulus of polycrystalline stishovite was obtained using acoustic velocity and density which were measured in this study.

Figure 10 shows the acoustic velocity data for stishovite obtained in this and previous

298 studies. The acoustic velocities of polycrystalline stishovite under nonhydrostatic
299 conditions are comparable to the aggregate velocity obtained from the measured acoustic
300 velocity of single-crystal stishovite under hydrostatic conditions by Jiang et al. (2009) and
301 to predictions by Karki et al. (1997) and Carpenter et al. (2000) before the transition. The
302 transverse velocity drop around 25 GPa in this study is about 3%, which is much smaller
303 than the velocity reduction of 60% that is predicted under hydrostatic conditions at 50 GPa
304 by ab initio calculations.
305 As for a confirmation of present result, we conducted a preliminary experiment using
306 diamond anvils with 450 μm culets without X-ray diffraction measurements. Transverse
307 velocity was measured with Brillouin scattering in a pressure range of 15–40 GPa. The
308 transverse velocity minimum was observed at around 27 GPa with 1.6% velocity reduction
309 (see supplemental figure 2). The absolute values of measured transverse velocity are
310 approximately 100 m/sec higher than those of present experiments. It might be due to the
311 difference of stress conditions and/or grain size in the sample.
312
313 **DISCUSSION**
314 A linear fit to the symmetry-breaking strain values and the pressure of the transverse

315 velocity minimum indicate a transition pressure between 25 and 35 GPa in present study.
316 This transition pressure is considerably lower than the values which reported in previous
317 X-ray diffraction studies for single crystal SiO_2 (stishovite) under quasi-hydrostatic
318 conditions (Hemley et al. 2000) and for polycrystalline SiO_2 (stishovite) using the laser
319 annealing method (Andrault et al. 2003). The lower transition pressure observed in the
320 present study might be caused by relatively large deviatoric stress in the sample, although
321 the laser annealing method used in the present study was similar to that of Andrault et al.
322 (2003). A stress condition is estimated as a pivotal pressure gradient (2 GPa/50 μm at 39
323 GPa with a NaCl-B2 pressure gauge) in present study. The estimated pressure gradient is a
324 lower bound due to the low shear strength of NaCl. The high shear strength of SiO_2 may
325 allow higher shear stress to be stored than that inferred from NaCl. Sintered polycrystalline
326 stishovite, which was synthesized and recovered from a high-pressure and high-temperature
327 experiment, was used as a starting material in the present study, whereas in situ synthesized
328 stishovite was used in Andrault et al. (2003). It is plausible that the difference in sample
329 preparation methods caused the difference in stress distribution in the sample because of
330 the high shear strength of stishovite. Furthermore, Andrault et al. (2003) conducted laser
331 annealing at 2300 K to attain almost hydrostatic conditions, whereas, in the present study,

laser annealing was conducted below the temperature threshold at which irradiation started, in order to prevent grain growth. The post-stishovite transition is known to be strongly affected by a deviatoric stress (e.g., Tsuchida and Yagi 1989), and the high shear strength of stishovite causes large deviatoric stresses under nonhydrostatic conditions (e.g., Hemley et al. 2000). Dubrovinsky and Belonoshiko (1996) showed that even small deviatoric stress could affect the post-stishovite phase transition. The method of identification of transitional pressure in the present study was the same as that in Andrault et al. (2003). Therefore, the difference in a stress condition is likely to be one of the main sources for lower transition pressure obtained in this study.

The results of this study are also inconsistent with the results of a radial X-ray diffraction experiment conducted under nonhydrostatic conditions by Shieh et al. (2002). They reported that the differential strain in the sample was around 4.5 GPa below 40 GPa and decreased to a minimum at around 48 GPa. Therefore, the displacive transition occurred at approximately 48 GPa, although the volume began to deviate from the values under nonhydrostatic conditions at around 20 GPa in the case of Shieh et al. (2002). We consider that the differences between the present study and that by Shieh et al. (2002) resulted from different stress distributions in the samples. This is plausible, because Shieh

et al. (2002) used synthesized powder without a pressure medium and did not conduct laser annealing, whereas the present study used a sintered pellet with a NaCl pressure medium and moderate laser annealing. Volume differences between the values obtained under hydrostatic conditions and under deviatoric stress were approximately 3% in present study, and approximately 2% in Shieh et al. (2002). It may imply that deviatoric stress condition in present study is relatively larger than the value of 4.5 GPa observed in the experiment by Shieh et al. (2002). Acoustic velocity measurements under controlled stress conditions with dense X-ray diffraction data, hopefully with a radial X-ray diffraction method, should be conducted to examine this inference.

If the observed velocity minima at around 22 GPa marks the beginning of transition, it takes about 18 GPa for the $CaCl_2$ phase to reach a transverse velocity value comparable to the one of the stishovite before softening. This pressure range is much larger than that reported by previous studies; 0 GPa reported with ab initio calculation for pure SiO_2 by Karki et al. (1997), around 5 GPa for experimental observation on hydrous alumina bearing SiO_2 by Lakshtanov et al. (2007), around 11 GPa suggested using a Landau free energy expansion for pure SiO_2 by Carpenter et al. (2000). In the present study, the acoustic velocity of polycrystalline SiO_2 was measured. Therefore, the obtained velocity is an

366 average of each SiO_2 grain. The small velocity drop observed in the present study may
367 indicate that the phase transition was gradual and corresponded to heterogeneous stress
368 distribution at intergranular contacts in the sample; as a result, the strong elastic softening
369 feature of post-stishovite transition was suppressed. The relatively large pressure interval of
370 velocity rebound might also be a result of overlapping of velocity minima in individual
371 grains, Partial dislocations associated with the shear induced phase transition may also
372 affect the reduction of velocity change across the transition (e.g., Putonis 1992). There is no
373 clear difference between the data measured along compression path and decompression
374 path in present result. Consistent absolute values might imply that grain size in the sample
375 didn't change apparently during compression. However, the hysteresis of transition
376 pressure might exist at least for the difference of stress condition between compression path
377 and decompression path. When we examine the data on compression and decompression
378 separately, compression data indicates that velocity minima may exist between 20 GPa and
379 30 GPa and decompression data indicates velocity minima may exist between 10 GPa and
380 20 GPa. In present study, deviatoric stress seems to suppress clear transition features of the
381 post stishovite phase transition. To discuss about hysteresis and the change of elastic
382 properties accompanying by the post-stishovite phase transition, hydrostatic experiments

383 should be conducted with dense X-ray diffraction and acoustic velocity measurements.

384 It is predicted that even a few volume percent of free silica can provide observable
385 seismic reflections in the mid-lower mantle because of the anomalous reduction in shear
386 velocity associated with the post-stishovite phase transition (Karki et al. 1997). A basaltic
387 layer in the subducting slab contains about 10–25 vol% of free SiO_2 in the deep mantle
388 region (e.g. Ono et al., 2001). Therefore, a seismic anomaly could be observed as a general
389 feature where subducting or upwelling oceanic crust exists. In fact, there are several
390 seismic reflectors at 800–1800 km depth which may be related to the post-stishovite phase
391 transition (Kawakatsu and Niu 1994; Le Stunff et al. 1995; Kaneshima and Helffrich 1999,
392 2010; Vinnik et al. 2001; Niu et al. 2003; Kaneshima 2009; Vinnik et al. 2010). Several
393 individual groups have investigated the phase boundary between stishovite and the
394 $CaCl_2$-structured phase at high temperature, and the results were rather controversial due to
395 difficulties in phase determination and choice of pressure scales, and the effect of deviatoric
396 stress (e.g., Kingma et al. 1995; Ono et al. 2002; Tsuchiya et al. 2004; Nomura et al. 2010).
397 Most recently, Nomura et al. (2010) determined the phase boundary at temperatures of
398 300–2500 K using a laser-heated diamond anvil cell experiment; they determined the phase
399 boundary to be at 50 GPa at 300 K with a positive Clapeyron slope of 11.1 MPa/K. The

transitional pressure in the pure SiO_2 system was found at 56–70 GPa for typical slab and mantle geotherms, which corresponds to the reflectors at a depth of around 1500 km (Kaneshima and Helffrich 1999, 2010) in the mantle and is still higher than the pressure corresponding to the reflectors at 800–1200 km depth. The effect of impurities such as Al and H in the SiO_2 phases is one of the possible explanations for the seismic reflectors at 800–1200 km depth (Lakshtanov et al. 2007), but this explanation does not exclude other possibilities such as compositional layering or decomposition of phase D (e.g., Kawakatsu and Niu 1994). A reduction in shear velocity across the post-stishovite transition as a result of Al or H impurities in stishovite is about 11% at a direction near [110] (Lakshtanov et al. 2007). The transition might be visible in seismic profiles if a subducting slab is under hydrostatic conditions. However, seismic observations indicating the occurrence of the post-stishovite transition accompanied with strong V_s reductions have only been observed locally, despite the large influence expected (Kaneshima and Helffrich 2010). Experimental investigation of the acoustic velocity in stishovite under hydrostatic conditions at high temperatures and pressures should be undertaken to clarify the nature of the post-stishovite phase transition. However, the present results may suggest that nonhydrostaticity in the subducting slab is one of the possible reasons for the absence of general seismic features in

417 the subducting slabs that clearly relate to the post-stishovite phase transition accompanied
418 by extremely low shear velocity anomalies. The present study reveals that nonhydrostatic
419 deviatoric stress reduces the transitional pressure and velocity change. Therefore, if the
420 post-stishovite phase transition occurs at lower pressures under nonhydrostatic stress, the
421 phase transition of stishovite containing some or no impurities does not occur at transitional
422 pressures with expected velocity reductions under hydrostatic conditions in the downgoing
423 slab. Silica-bearing layers such as basalts and sediments are likely to be stretched and
424 folded in the mid-lower mantle; therefore, a velocity change of less than 3% due to the
425 phase transition of stishovite might be obscured by anomalies caused by temperature
426 differences or chemical and structural heterogeneity. However, this phase transition of
427 stishovite under deviatoric stress could affect the generation of scattering objects in the
428 mid-lower mantle (e.g., Kaneshima and Helffrich 2010) and also could influence the
429 rheological behavior of a subducting slab, such as slab thickening observed in the
430 mid-lower mantle (Van der Hilst 1995; Shellart et al. 2009; Zhao 2004).

431 The deviatoric stress in the present study was estimated to be 2 GPa from pressure
432 distribution in the sample obtained using NaCl-B2 pressure gauge. However, the difference
433 between the volumes of stishovite obtained in this study and in previous studies under

hydrostatic conditions and under deviatoric stress implies that stress condition in stishovite was larger than a value about 4.5 GPa. This is in the possible stress range for a subducting slab based on the stress capacity of major constituent minerals (Chen 2010), although the actual stress conditions in the subducting slab are not known. According to the stress measurements for mantle phases (e.g. Weidner et al. 1998; Chen et al. 2010), differential stress decreases with increasing temperature. Weidner et al. (1998) demonstrated that microstrain in stishovite decreased to 80 % of initial strain with increasing temperature up to 1273 K at experimental pressure of 12 GPa. The experimental condition is close to the coesite-stishovite phase boundary (Akaogi et al. 1995). Stishovite has a wide stability field from 8 GPa to 60 GPa along the cold slab geotherms (e.g. Kirby et al. 1996) which corresponding to the range from the transition zone to the mid-lower mantle region of the earth, The stress capacity of stishovite under higher pressures is still unclear. Although the value depends on the mineral phases, the rate of reduction was estimated to be 60% and 20% at 20 GPa and 1073 K for ringwoodite and perovskite, respectively (Chen et al. 2010). This implies that the stress capacity of minerals is small under mid-lower mantle conditions. In the mid-lower mantle region, the stress conditions might be weaker than that in the region shallower than 700 km depth because of stress-reducing processes such as seismic

451 energy release and recrystallization annealing across the perovskite-forming reaction (e.g.,
452 Bina 2010). However, it is plausible that a certain deviatoric stress exists in silica-rich
453 layers even in the mid-lower mantle region, as a result of the high shear strength of
454 stishovite. The results presented here suggest the possibility that the post-stishovite phase
455 transition under deviatoric stress explains the lack of general seismic features of extreme
456 reductions in shear velocity related to the post stishovite transition in the mid-lower mantle.
457 The post stishovite transition which occurs at lower pressures under nonhydrostatic
458 conditions may affect the local seismic scattering structures and the rheological behavior of
459 subducting slabs, as displayed by slab-thickening features observed in the mid-mantle
460 region. The effect of stress on the transitional pressure and the elasticity change of
461 stishovite at high temperatures should be investigated with accurate stress estimation for
462 further discussion.
463
464

465 **ACKNOWLEDGEMENTS**

466 We thank K. Funakoshi, Y. Higo, and T. Matsuzaki for their help in sample preparation,
467 and K. Kudo, L. Dai, and T. Tsuchiya for valuable discussions. We also thank K. Nagaki

468 and K. Tanaka for their help in microprobe analysis. T. Sakai and A. Suzuki are appreciated
469 for their help in FT–IR measurement. We appreciate C. Bina and two anonymous reviewers
470 for constructive suggestions. T. Kondo and E. Ohtani are appreciated for their fundamental
471 support. Y. A. was partially supported by a JSPS research fellowship for young scientists.
472 This study was performed under the approval of the following proposal numbers:
473 2009B0087, 2010A0087, 2010B0087, and 2011A1440 of SPring-8. This study was
474 partially carried out under the Visiting Researcher's Program of the Institute for Study of
475 the Earth's Interior, Okayama University. The authors would like to thank Enago
476 (www.enago.jp) for the English language review.

477

478

REFERENCES CITED

Akahama, Y., Kawamura, H. (2006) Pressure calibration of diamond anvil Raman gauge to 310 GPa. Journal of Applied Physics, 100, 043516.

Akaogi, M., Akimoto, S. (1979) High pressure phase equilibria in a garnet lherzolite, with special reference to Mg^{2+}-Fe^{2+} partitioning among constituent minerals. Physics and the Earth and Planetary Interiors, 19, 31-51.

Akaogi, M., Yusa, H., Shiraishi, K., Suzuki, T. (1995) Thermodynamic properties of α-quartz, coesite, and stishovite and equilibrium phase relations at high pressures and high temperatures. Journal of Geophysical Reserch, 100, 22337-22347.

Andrault, D., Fiquet, G., Guyot, F., Hanfland, M. (1998) Pressure-induced Landau-Type Transition in Stishovite. Science, 282, 720-724.

Andrault, D, Angel, R.J., Mosenfelder, J.L., and Le Bihan, T. (2003) Equation of state of stishovite to lower mantle pressures. American Mineralogist, 88, 301-307.

Baer, B.J., Brown, J.M., Zaug, J.M., Schiferl, D., Chronister, E. (1998) Impulsive stimulated scattering in ice VI and ice VII. Journal of Chemical Physics, 108,

4540-4544.

Bina, C.R. (2010) Scale limits of free-silica seismic scatters in the lower mantle, Physics of the Earth and Planetary Interiors, 183, 110-114.

Brazhkin, V.V., McNeil, L.E., Grimsditch, L.E., Bendeliani, N.A., Dyuzheva, T.I., Lityagina, L.M. (2005) Elastic constants of stishovite up to its amorphization temperature. Journal of Physics: Condensed Matter, 17, 1869-1875.

Brown, J.M. (1999) The NaCl pressure standard. Journal of Applied Physics, 86, 5801-5808.

Carpenter, M., Hemley, M.A., Mao, H.K. (2000) High-pressure elasticity of stishovite and the P42/mnm–Pnnm phase transition. Journal of Geophysical Research, 105, 10807-10816.

Chen, J. (2010) Understanding depth variation of deep seismicity from in situ measurements of mineral strength at high pressures. Journal of Physics and Chemistry of Solids, 71, 1032-1037.

Cohen, R.E. (1992) First-principles predictions of elasticity and phase transitions in high pressure SiO_2 and geophysical implications. In: Syono, Y., Manghnani, M.H. (Eds.) High pressure research: Application to Earth and Planetary sciences. 425 p. AGU,

513 Washington, DC.

514 Dubrovinsky, L.S. and Belonoshiko, A.B. (1996) Pressure-induced phase transition and
515 structural changes under deviatoric stress of stishovite to $CaCl_2$-like structure.
516 Geochemica Cosmochemica Acta, 60, 3657-3663.

517 Gerward, L., Mørup, S., Topsøe, H. (1976) Particle size and strain broadening in
518 energy-dispersive x-ray powder patterns. Journal of Applied Physics, 47, 822-825.

519 Hemley, R.J., Shu, J., Carpenter, M.A., Hu, J., Mao, H.K., Kingma, K.J. (2000)
520 Strain/order parameter coupling in the ferroelastic transition in dense SiO_2. Solid
521 State Communications, 114, 527-532.

522 Jiang, F., Gwanmesia, G.D., Dyuzheva, T.D., Duffy, T.S. (2009) Elasticity of stishovite
523 and acoustic mode softening under high pressure by Brillouin scattering. Physics of
524 the Earth and Planetary Interiors, 172. 235-240.

525 Kaneshima, S., Helffrich, G. (1999) Dipping low-velocity layer in the mid-lower mantle:
526 evidence for geochemical heterogeneity. Science, 283, 1888-1891.

527 Kaneshima, S. and Helffrich, G. (2010) Small scale heterogeneity in the mid-lower
528 mantle beneath the circum-Pacific area. Physics of the Earth and Planetary Interiors,
529 183. 91-103.

530 Karki, B.B., Stixrude, L., Crain, J. (1997) Ab initio elasticity of three high-pressure
531 polymorphs of silica. Geophysical Research Letters, 24. 3269-3272.
532 Kawakatsu, H., Niu, F.L. (1994) Seismic evidence for a 920-km discontinuity in the
533 mantle. Nature, 371, 301-305.
534 Kingma, K.J., Cohen, R.E., Hemley, R.J., Mao, H.K. (1995) Transformation of
535 stishovite to a denser phase at lower-mantle pressures. Nature, 374, 243-245.
536 Kirby, S.H., Stein, S., Okal, E.A., Rubie, D.C. (1996) Metastable mantle phase
537 transformations and deep earthquakes in subducting oceanic lithosphere. Reviews of
538 Geophysics, 34, 261-306.
539 Klug, H.P. and Alexander, H.P. (1974) Crystallite size and lattice strains from line
540 broadening. In X-ray diffraction procedures, 2nd ed., p. 618-708. Wiley, New York.
541 Lakshtanov, D.L., Sinogeikin, S.V., Litasov, K.D., Prakapenka, V.B., Hellwig, H., Wang,
542 J., Sanches-Valle, C., Perrillat, J.P., Chen, B., Somayazulu, M., Li, J., Ohtani, E.,
543 Bass, J.D. (2007) The post-stishovite phase transition in hydrous alumina-bearing
544 SiO_2 in the lower mantle of the earth. Proceedings of the National Academy of
545 Science, 104, 13588-13590.
546 Le Stunff, Y., Wicks Jr., C.W., Romanowicsz, B. (1995) P'P' Precursors under Africa:

547 Evidence for mid-mantle reflectors. Science, 270, 74-77.

548 Mao, H.K., Bell, P.M., Shaner, W.G., Steinberg, D.J. (1978) Specific volume
549 measurements of Cu, Mo, Pd, and Ag and calibration of the ruby R1 fluorescence
550 pressure gauge from 0.06 to 1 Mbar. Journal of Applied Physics, 49, 3276-3283.

551 Marquardt, H., Gleason, A., Marquardt, K., Speziale, S., Miyagi, L., Neusser, G., Wenk,
552 H.-R., Jeanloz, R. (2011) Elastic properties of MgO nanocrystals and grain
553 boundaries at high pressures by Brillouin scattering. Physical Review B, 84,
554 064131.

555 Niu, F., Kawakatsu, H., Fukao, Y. (2003) Seismic evidence for a chemical heterogeneity
556 in the midmantle: A strong and slightly dipping seismic reflector beneath the
557 Mariana subduction zone. Journal of Geophysical Research, 108,
558 doi:10.1029/2002JB002384.

559 Nomura, R., Hirose, K., Sata, N., Ohishi, Y. (2010) Precise determination of
560 post-stishovite phase transition boundary and implications for seismic
561 heterogeneities in the mid-lower mantle. Physics of the Earth and Planetary Interiors,
562 183, 104-109.

563 Ohishi, Y., Hirao, N., Sata, N., Hirose, K., Takata, M. (2008) Highly intense

monochromatic X-ray diffraction facility for high-pressure research at SPring-8. High Pressure Research, 28, 163-173.

Ono, S., Ito, E., Kastura, T. (2001) Mineralogy of subducted basaltic crust (MORB) from 25 to 37 GPa, and chemical heterogeneity of the lower mantle. Earth and Planetary Science Letters, 190, 57-63.

Ono, S., Hirose, K., Murakami, M., Isshiki, M. (2002) Post-stishovite phase boundary in SiO_2 determined by in situ X-ray observations. Earth and Planetary Science Letters, 197, 187-192.

Putonis, A. (1992) Twin boundaries. In Introduction to Mineral Sciences, p. 223-234. Cambridge university press, Cambridge.

Ross, N.L., Shu, J.F., Hazen, R.M., Gasparik, T. (1990) High pressure crystal chemistry of stishovite. American Mineralogist, 75, 739-747.

Sakai, T., Ohtani, E., Hirao, N., Ohishi, Y. (2011) Equation of state of the NaCl-B2 phase up to 304 GPa. Journal of Applied Physics, 109, 084912.

Shellart, W.P., Freeman, J., Stegman, D.R., Moresui, L., May, D. (2009) Evolution and diversity of subduction zones controlled by slab width. Nature, 446, 308-311.

Shieh, S.R., T.S. Duffy, Li, B. (2002) Strength and elasticity of SiO_2 across the

Stishovite–$CaCl_2$-type structural phase boundary. Physical Review Letters, 89, 255507.

Shimizu, H., Ohnishi, M., Sasaki, S. (1995) Cauchy relation in dense H_2O ice VII. Physical Review Letters, 74, 2820-2823.

Tsuchida, Y. and Yagi, T. (1989) A new, post stishovite high-pressure polymorph of silica. Nature, 340, 217-220.

Tsuchiya, T., Caracas, R., Tsuchiya, J. (2004) First principles determination of the phase boundaries of high-pressure polymorphs of silica. Geophysical Research Letters, 31, L11610, doi: 10.1029/2004GL019649.

Van der Hilst, R. (1995) Complex morphology of subducted lithosphere in the mantle benearth the Tonga trench. Nature, 374, 154-157.

Vinnik, L., Kato, M., Kawakatsu, H. (2001) Search for seismic discontinuities in the lower mantle. Geophysical Journal International, 147, 41-56.

Vinnik, L.P., Oreshin, S.I., Speziale, S., Weber, M. (2010) Mid-mantle layering from SKS receiver functions. Geophysical Research Letters, 37, L24302.

Weidner, D.J., Bass, J.D., Ringwood, A.E., Sinclair, W. (1982) The single-crystal elastic moduli of stishovite. Journal of Geophysical Research, 87, 4740-4746.

598 Weidner, D.J., Wang, Y., Chen, G., Ando, J., Vaughan, M.T. (1998) Rheology
599 measurement at high pressure and temperature. In M.H. Manghnani, and T. Yagi,
600 Eds., Properties of Earth and Planetary Materials at Pressure and Temperature,
601 Gephysical Monograph 101, p. 473-482. American Geophysical Union, Washington,
602 D.C.
603 Yoneda, A. and Song, M. (2005) Frequency domain analysis of ultrasonic velocity: An
604 alternative bond effect correction constraining bond properties. Journal of Applied
605 Physics, 97, 024908.
606 Zhao, D. (2004) Global tomographic images of mantle plumes and subducting slabs:
607 insight into deep earth dynamics. Physics of Earth and Planetary Interiors, 146,
608 3-34.
609
610

611 **Figure captions**

612

613 Figure 1. Photograph of a SiO_2 sintered pellet confined within the NaCl pressure
614 medium in the diamond anvil cell at 300 K and 40 GPa.

615

616 Figure 2. The relation between pressures obtained with the internal pressure scales of
617 ruby and NaCl against the pressure obtained with the Raman edge frequency shift of a
618 diamond culet.

619

620 Figure 3. A representative Brillouin spectrum corrected at 56 GPa and room temperature.

621

622 Figure 4. Acoustic velocities in polycrystalline stishovite measured in this study as a
623 function of pressure: A) longitudinal velocities; B) transverse velocities. Filled circles and
624 open squares represent acoustic velocities measured along compression and decompression
625 paths, respectively. The uncertainties of the obtained velocity were calculated from
626 uncertainty of peak fitting and standard deviation of averaged data.

627

628 Figure 5. Representative integrated X-ray diffraction profiles of the sample (SiO_2 and
629 NaCl) at room temperature and pressures of (a) 1 GPa, (b) 16 GPa, (c) 39 GPa, and (d) 60
630 GPa. Abbreviations of peaks are as follows: R, Rutile-type SiO_2; C, $CaCl_2$-type SiO_2; B1,
631 B1-type NaCl.
632
633 Figure 6. Square of the symmetry-breaking strain through the transition. Open and filled
634 circles, the data obtained in this study for the rutile-structure phase and the $CaCl_2$-type
635 phase, respectively; crosses and open squares, the data obtained by Andrault et al., (2003)
636 for the rutile-structure phase and the $CaCl_2$-type phase, respectively. The bold dashed line
637 and the solid line are a fit to the data for the $CaCl_2$-structured phase obtained in this study
638 and Andrault et al., (2003), respectively; the thin dashed line is a horizontal line for zero.
639
640 Figure 7. Volumes (A) and lattice parameters of SiO_2 phases as a function of pressure for
641 a and b axes (B), and for c axes (C). Open circles, lattice parameters for the rutile-type
642 phase obtained in this study; filled diamonds and filled circles, lattice parameters for the
643 $CaCl_2$-type phase obtained in this study; Crosses and gray filled triangles, lattice parameters
644 for the rutile-type phase obtained by Andrault et al., (2003) and Ross et al., (1990),

645 respectively. Open triangles and open squares, lattice parameters for the $CaCl_2$-type phase
646 obtained by Andrault et al. (2003).
647
648 Figure 8. The FWHM of polycrystalline stishovite as a function of 2 theta at 1 GPa. The
649 curve shows a fitting result on these data to equation 1? with the weighted least square
650 method.
651
652 Figure 9. The approximate upper limit of strain obtained from the FWHM analysis a) as
653 a function of pressure, b) as a function of d value. Relatively large values of upper limit of
654 strain for hkl = (101) corresponding to the d-value of around 2.2 Å are due to
655 contamination of hkl = (011) above 30 GPa.
656
657 Figure 10. Acoustic velocities in SiO_2 phases as a function of pressure. Filled circles and
658 open squares, longitudinal velocities measured in this study along compression and
659 decompression paths, respectively; open circles and filled squares, transverse velocities
660 measured in this study along compression and decompression paths, respectively; open
661 diamonds and open triangles, longitudinal and transverse velocities for aggregate obtained

662 from the measurement data for single crystal SiO_2 by Jiang et al., (2009); solid triangles,
663 acoustic velocities close to the [110] phonon direction of hydrous alumina bearing
664 stishovite measured by Lakshtanov et al. (2007); gray dashed lines, aggregate velocity
665 predicted by a Landau free energy calculation by Carpenter et al. (2000); solid lines,
666 polynomial fit to the longitudinal velocities and transverse velocities measured in this study,
667 respectively. Polynomial fits were made separately on transverse velocity at pressures
668 below and above 25 GPa. The longitudinal velocities didn't treat separately as transverse
669 velocity because the data were not sufficient due to overlapping with diamond transverse
670 velocity (see text): the gray dotted line is a visual guide for the measured velocities for Al-
671 and H-bearing SiO_2.
672
673 Supplementary figure 1. A representative 2-dimensional X-ray diffraction image
674 obtained at 1 GPa and room temperature.
675
676 Supplementary figure 2. Transverse acoustic velocities in polycrystalline stishovite
677 measured in this study as a function of pressure: The values obtained in an additional
678 experiment are plotted as gray circles. The velocity minimum is observed around 27 GPa.

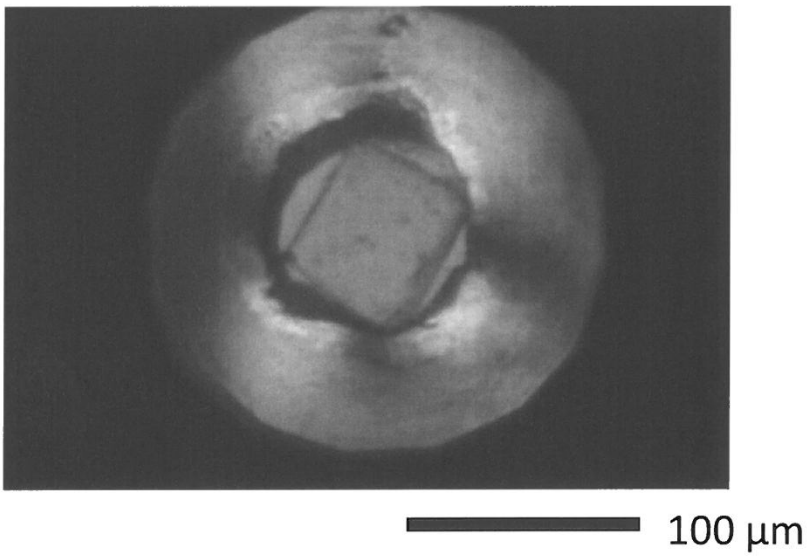

Fig.1

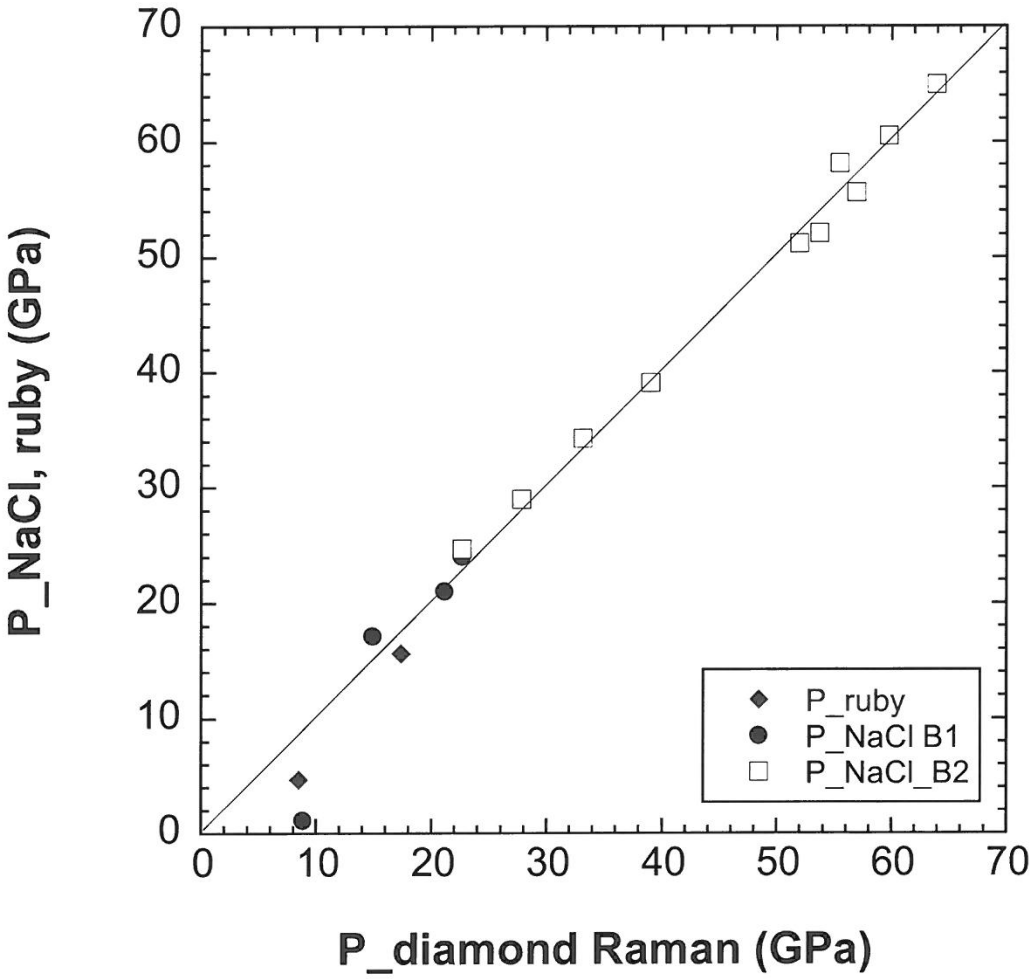
P_NaCl, ruby (GPa)
P_diamond Raman (GPa)
P_ruby
P_NaCl B1
P_NaCl_B2
0
10
20
30
40
50
60
70

Fig. 2

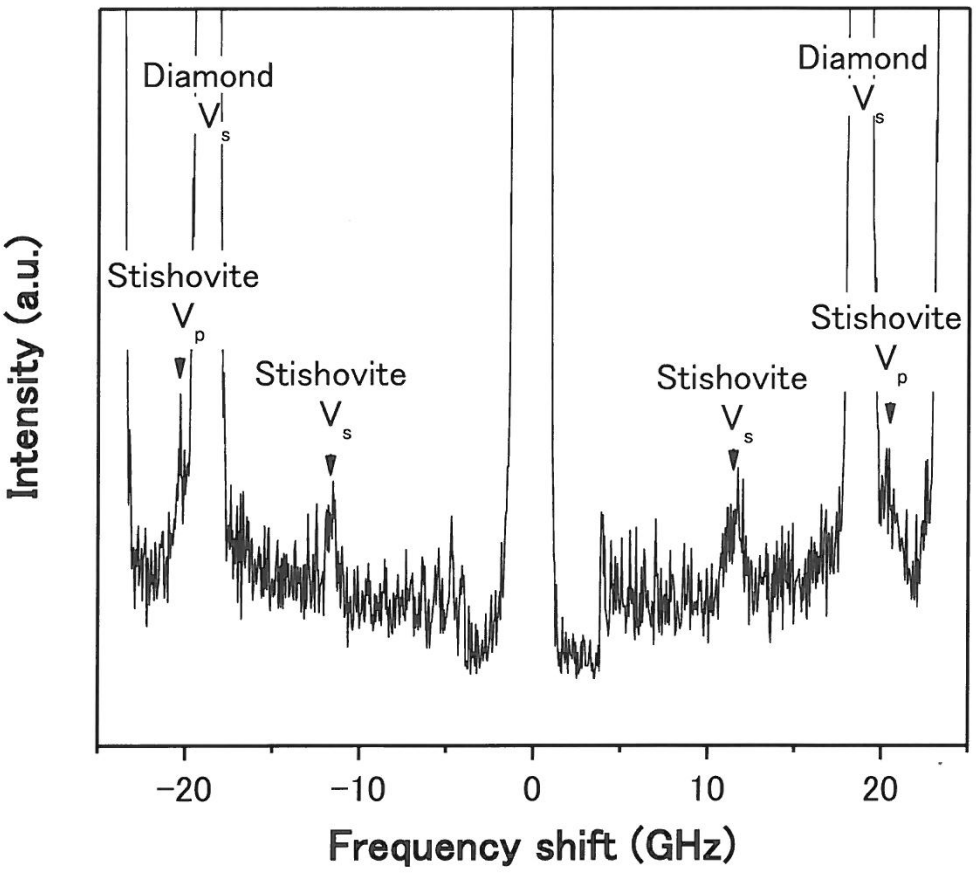
Diamond
V_s
Stishovite
V_p
Stishovite
V_s
Diamond
V_s
Stishovite
V_s
Stishovite
V_p
Intensity (a.u.)
−20
−10
0
10
20
Frequency shift (GHz)

Fig. 3

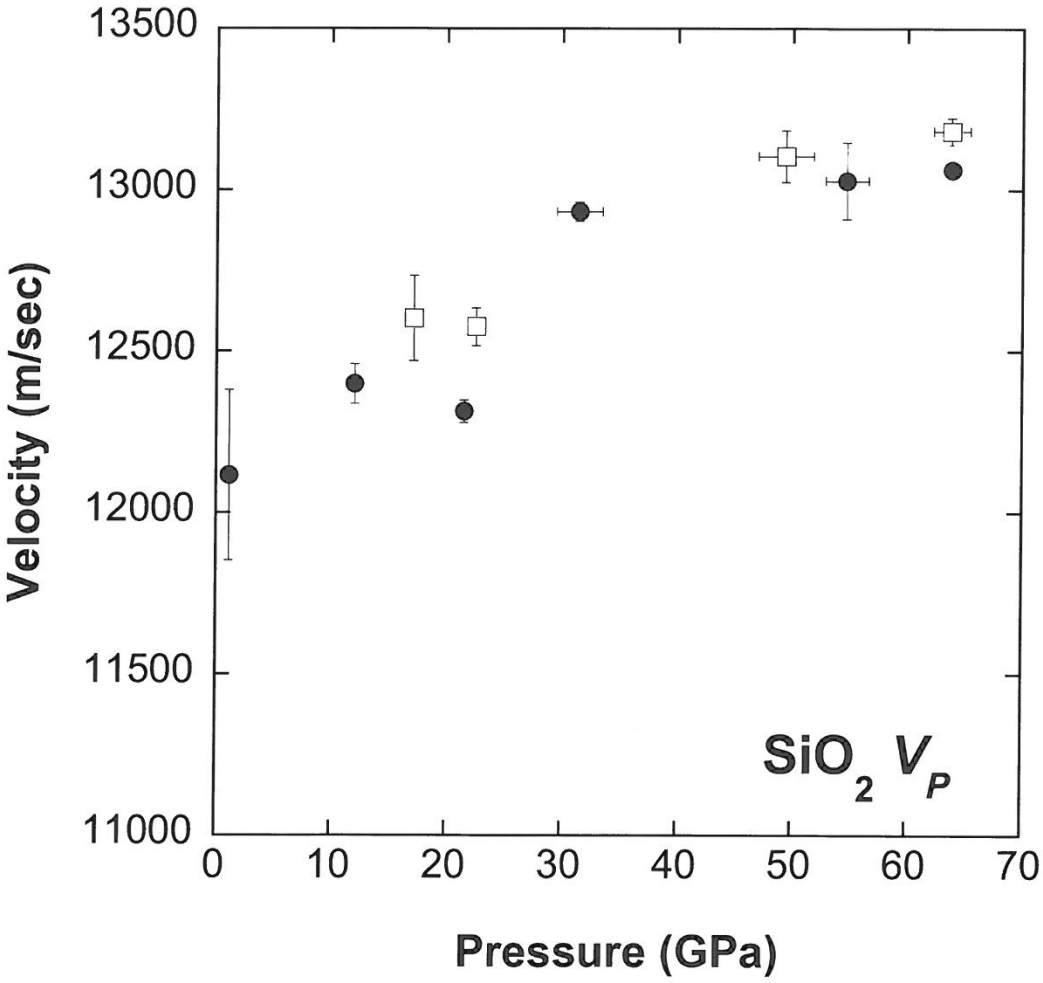
13500
13000
12500
12000
11500
11000
Velocity (m/sec)
0
10
20
30
40
50
60
70
Pressure (GPa)
SiO2 VP

Fig.4a

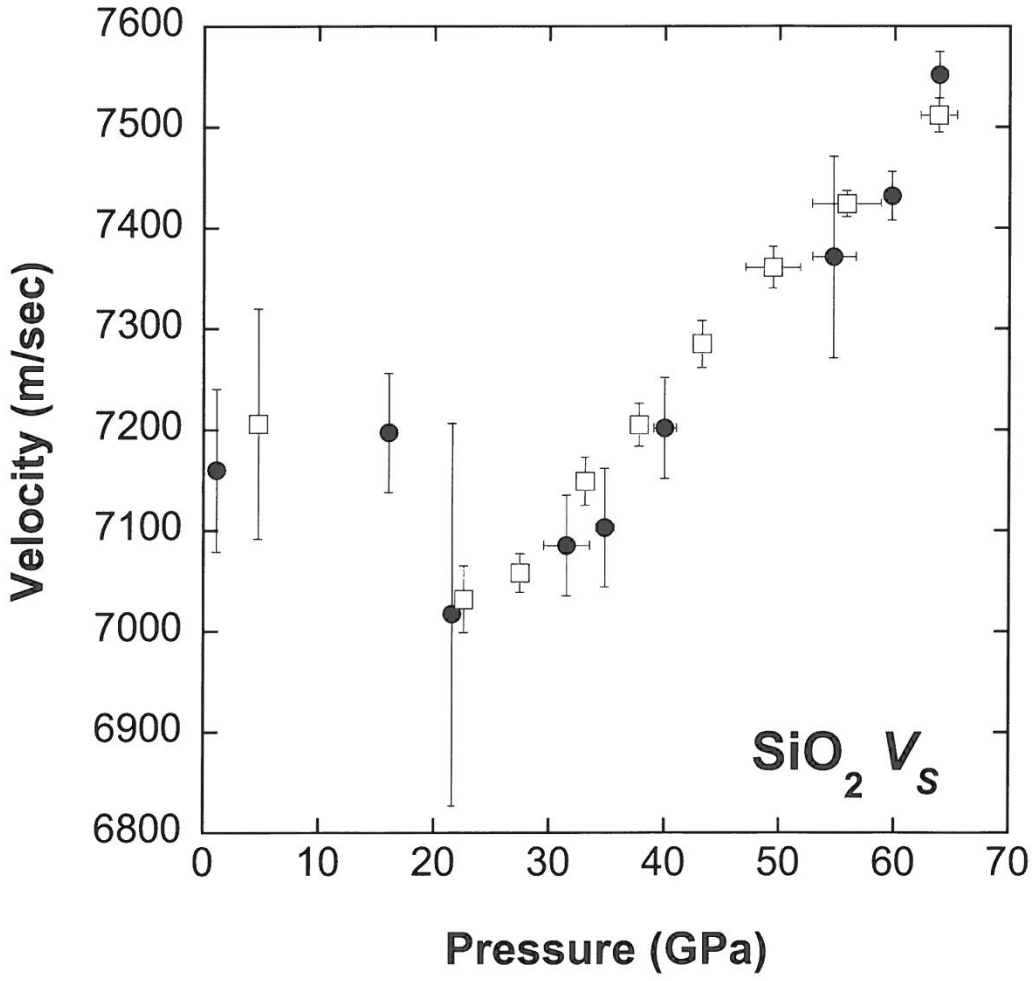
7600
7500
7400
7300
7200
7100
7000
6900
6800
Velocity (m/sec)
0
10
20
30
40
50
60
70
Pressure (GPa)
SiO2 VS

Fig. 4b

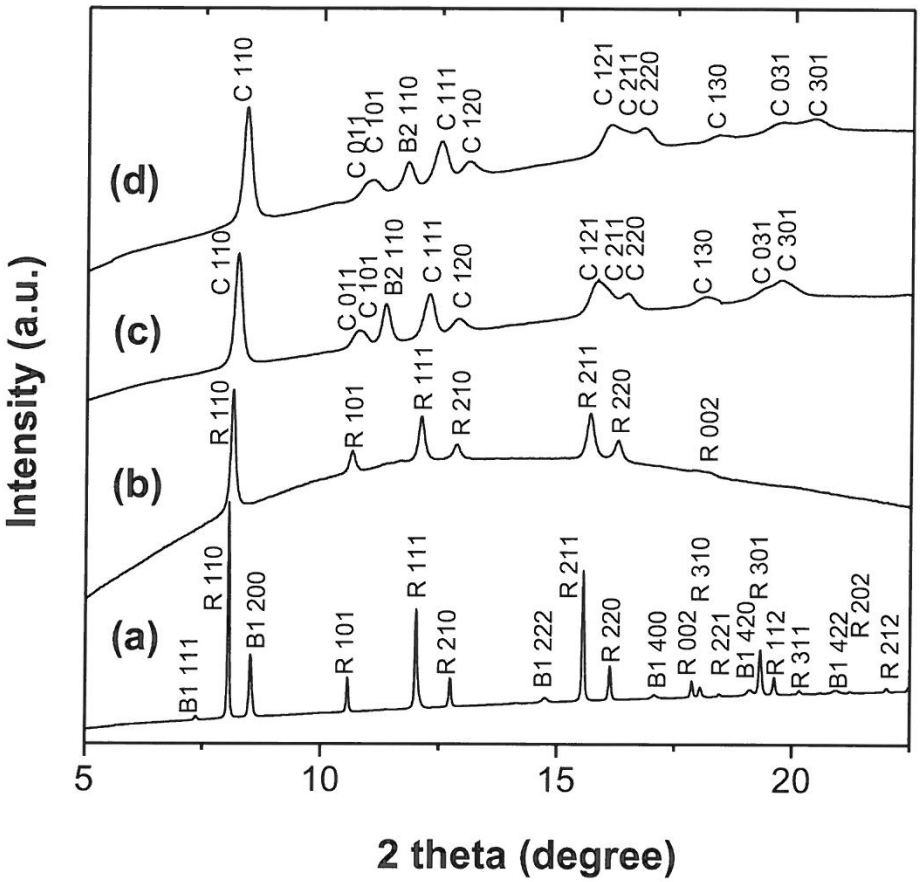
Intensity (a.u.)
2 theta (degree)
5
10
15
20
(a)
(b)
(c)
(d)
B1 111
R 110
B1 200
R 101
R 111
R 210
B1 222
R 211
R 220
B1 400
R 002
R 310
R 221
B1 420
R 301
R 112
R 311
B1 422
R 202
R 212
R 101
R 111
R 210
R 211
R 220
R 002
C 110
C 011
C 101
B2 110
C 111
C 120
C 121
C 211
C 220
C 130
C 031
C 301

Fig.5 r2

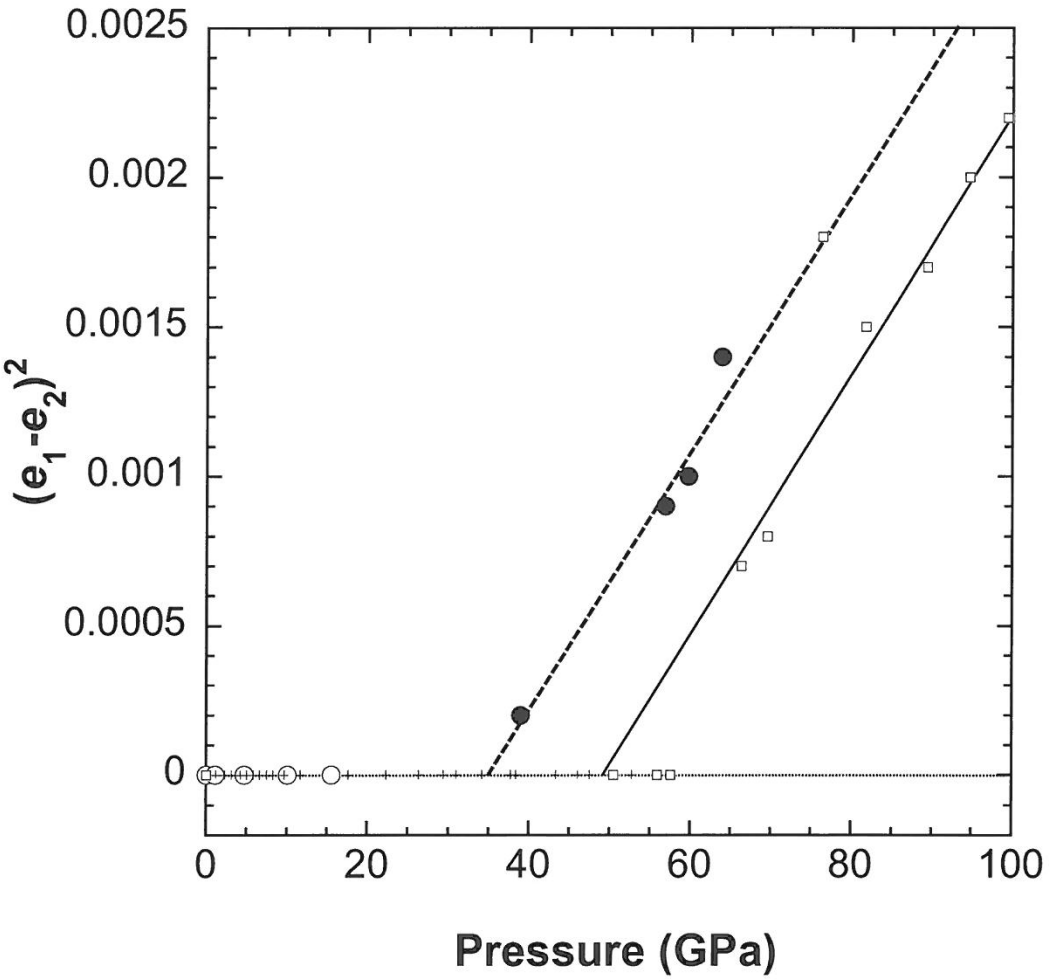
0.0025
0.002
0.0015
0.001
0.0005
0
$(e_1-e_2)^2$
0
20
40
60
80
100
Pressure (GPa)

Fig. 6

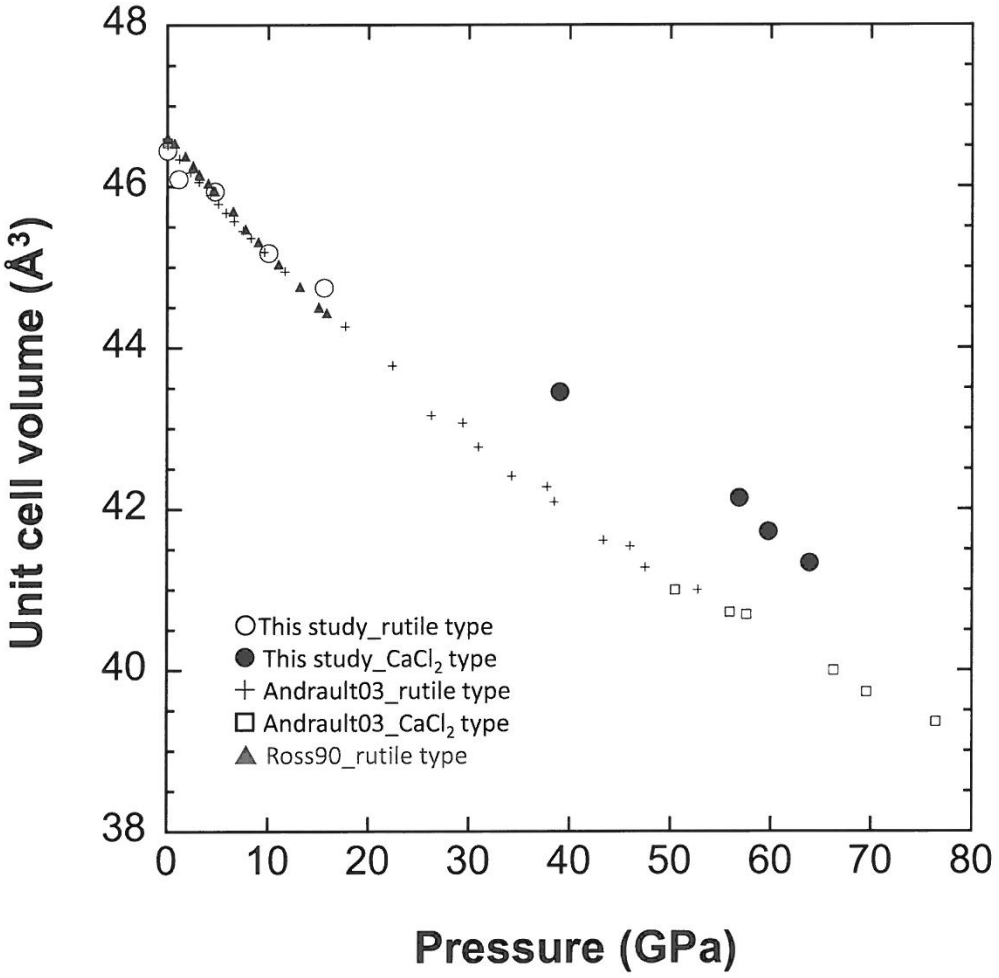
Unit cell volume (Å³)
Pressure (GPa)
48
46
44
42
40
38
0
10
20
30
40
50
60
70
80
This study_rutile type
This study_CaCl2 type
Andrault03_rutile type
Andrault03_CaCl2 type
Ross90_rutile type

Fig. 7a

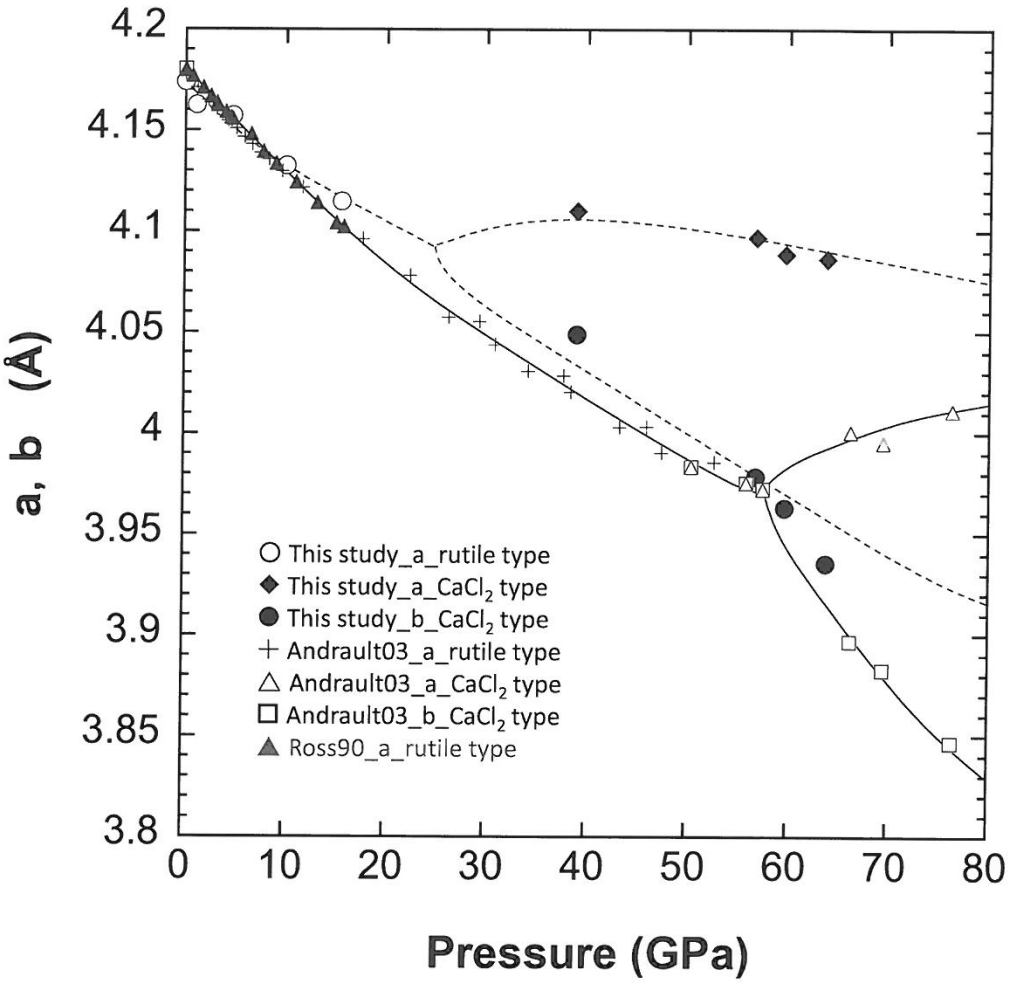
4.2
4.15
4.1
4.05
4
3.95
3.9
3.85
3.8
a, b (Å)
0
10
20
30
40
50
60
70
80
Pressure (GPa)
This study_a_rutile type
This study_a_CaCl2 type
This study_b_CaCl2 type
Andrault03_a_rutile type
Andrault03_a_CaCl2 type
Andrault03_b_CaCl2 type
Ross90_a_rutile type

Fig. 7b

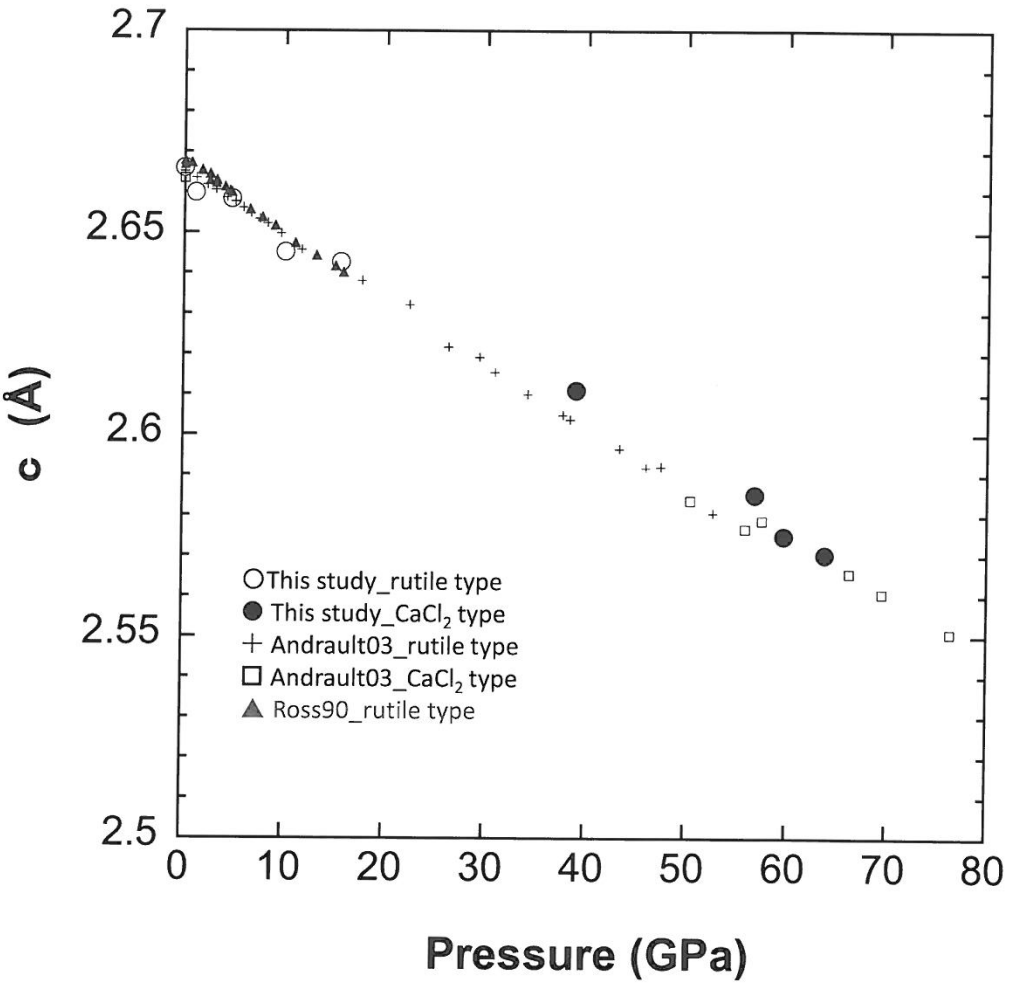
2.7
2.65
2.6
2.55
2.5
c (Å)
0
10
20
30
40
50
60
70
80
Pressure (GPa)
This study_rutile type
This study_CaCl2 type
Andrault03_rutile type
Andrault03_CaCl2 type
Ross90_rutile type

Fig. 7c

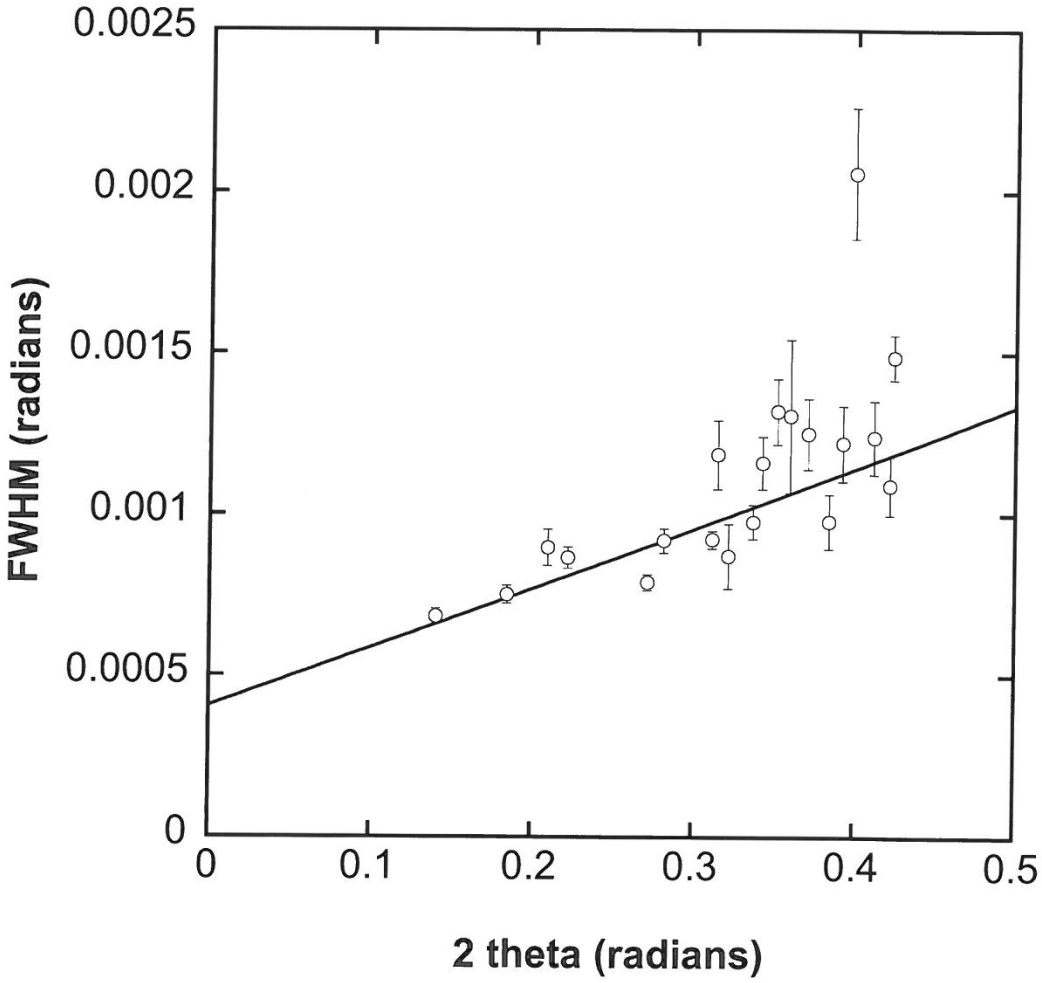
0.0025
0.002
0.0015
0.001
0.0005
0
FWHM (radians)
0
0.1
0.2
0.3
0.4
0.5
2 theta (radians)

Fig 8 r2

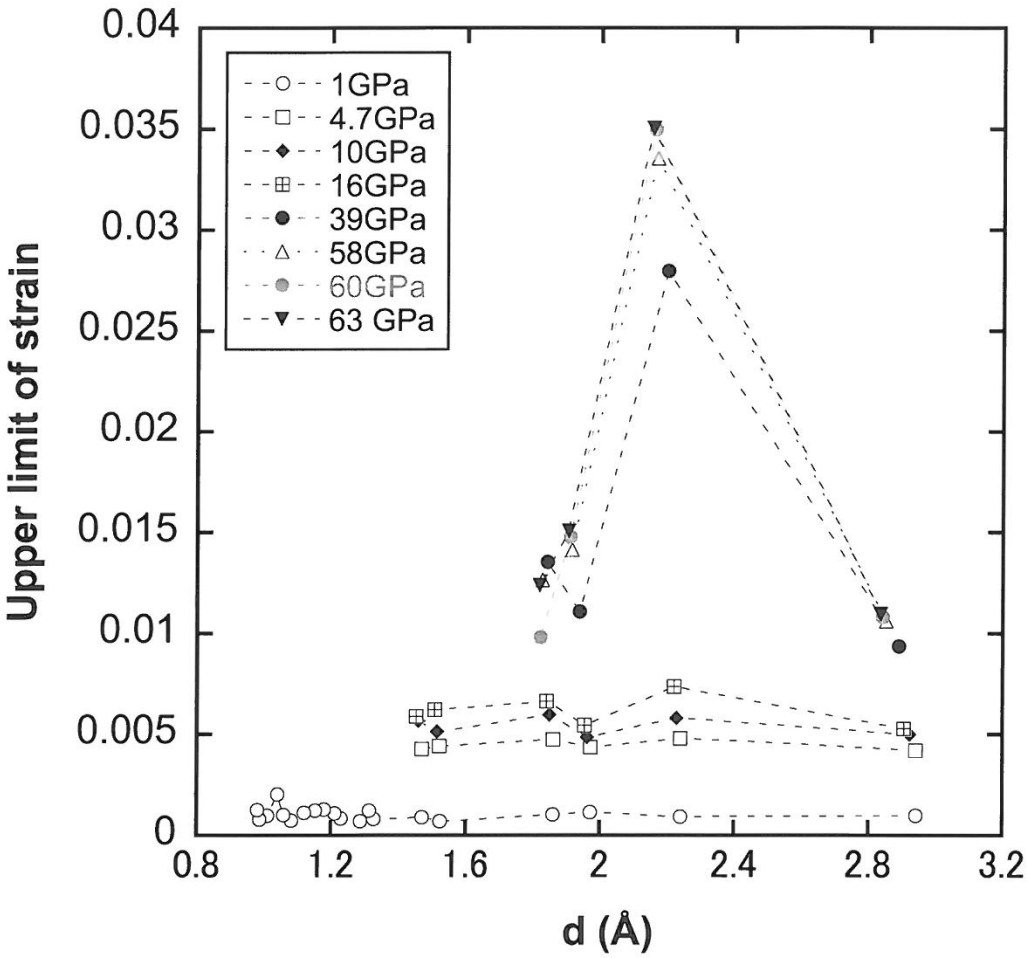
0.04
0.035
0.03
0.025
0.02
0.015
0.01
0.005
0
Upper limit of strain
1GPa
4.7GPa
10GPa
16GPa
39GPa
58GPa
60GPa
63 GPa
0.8
1.2
1.6
2
2.4
2.8
3.2
d (Å)

Fig 9a r3

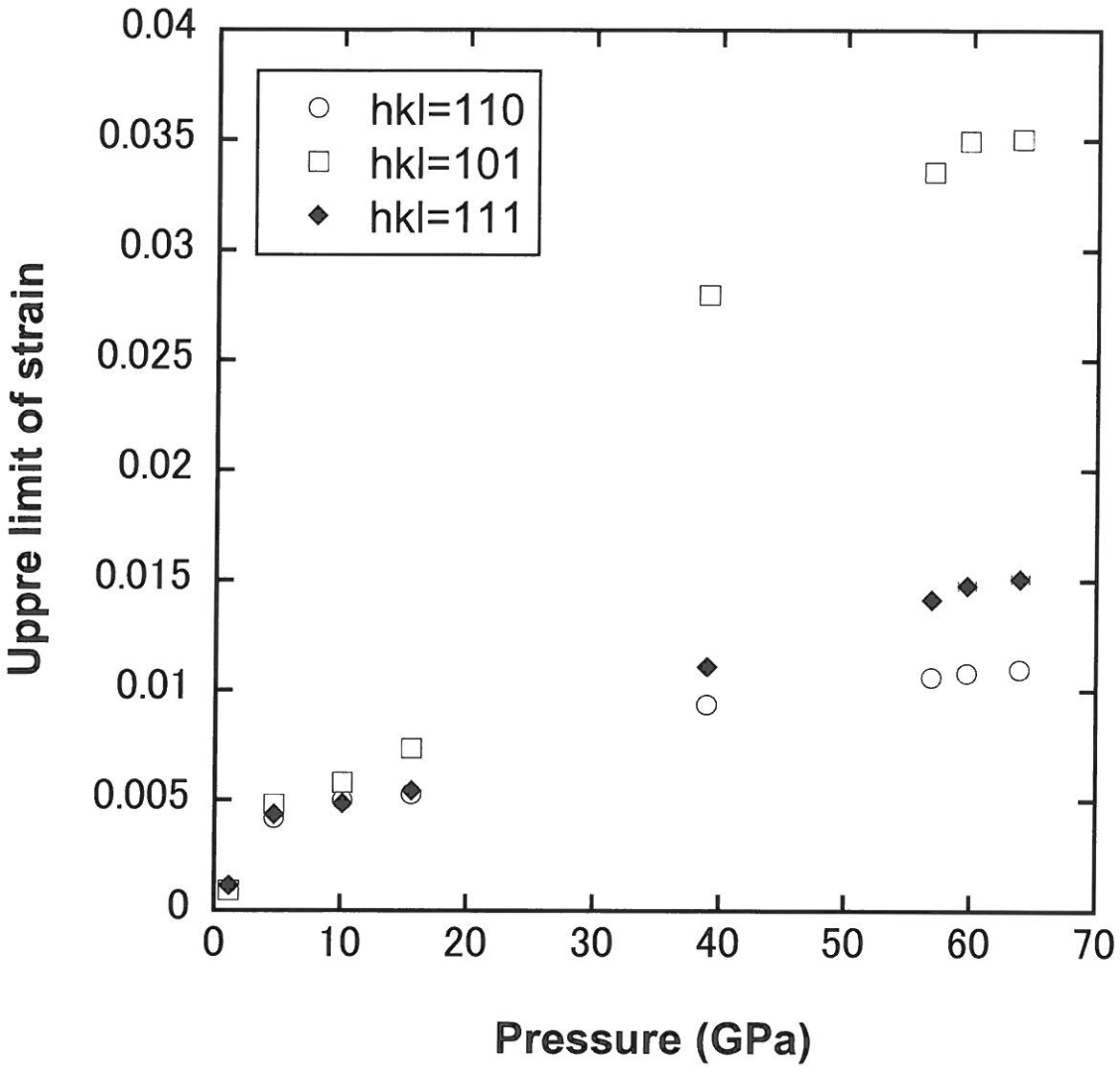
hkl=110
hkl=101
hkl=111
Uppre limit of strain
Pressure (GPa)
0.04
0.035
0.03
0.025
0.02
0.015
0.01
0.005
0
0
10
20
30
40
50
60
70

Fig 9b r3

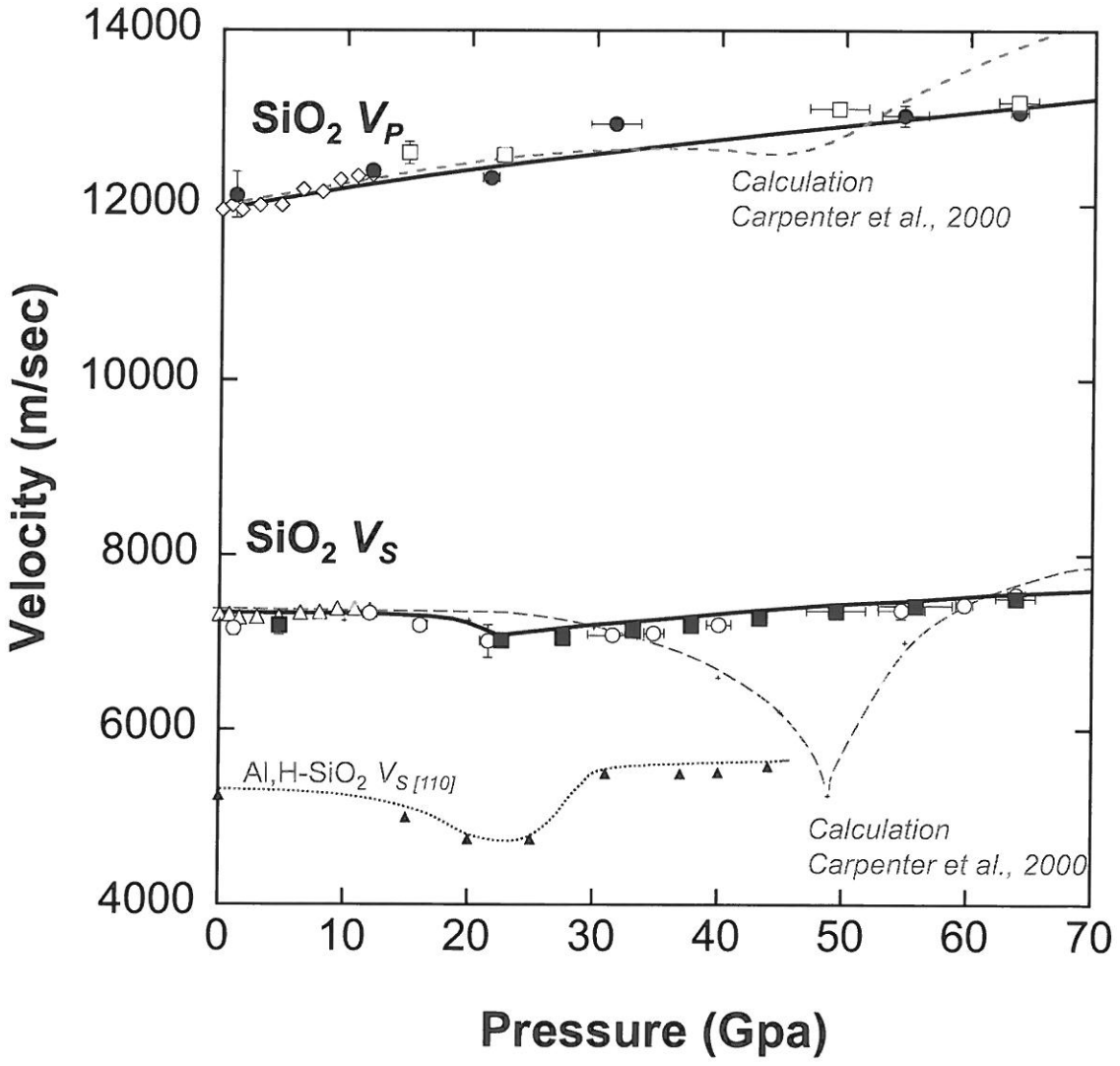
14000
12000
10000
8000
6000
4000
Velocity (m/sec)
SiO2 VP
Calculation
Carpenter et al., 2000
SiO2 VS
Al,H-SiO2 VS [110]
Calculation
Carpenter et al., 2000
0
10
20
30
40
50
60
70
Pressure (Gpa)

Fig. 10 r2